Progress In Electromagnetics Research C, Vol. 129, 35–50, 2023

Beam-Steering for Narrow Beamwidth 120 GHz Antenna Array Using Deep Learning for Radar Application

Ahmed M. Montaser*

Abstract—The narrow beam-width 120 GHz industry, scientific, and medical band compact substrate integrated waveguide (SIW) driven antenna's design and characterization are discussed in this study. A low-cost fabrication is ensured by the employment of a single RO4350B substrate layer with SIW feeding. A transition from SIW to a rectangular waveguide is made for measuring purposes. The radiation pattern has been measured. By determining the right feeding phases for the 20 elements, a Deep Neural Network (DNN) is used to softly compute the beam steering. The weighted hybrid Modified Gravitational Search Algorithm (MGSA) — Particle Swarm Optimization (PSO) approach and neural network with back-propagation technique are utilized to beam-steer by anticipating the appropriate feeding phases of the antenna array elements. To evaluate the effectiveness of the approaches, a number of sample instances are given that beam-steer the pattern in a variety of directions. In addition to allowing for the establishment of crucial analytical equations for the synthesis of antenna arrays, the neural network synthesis method also offers a great deal of flexibility between the system parameters in input and output, which makes the synthesis possible due to the explicit relationship given by them. The conventional technique of the phased array is compared with our DNN model for implementing beam steering.

1. INTRODUCTION

Due to license-free access, high frequency, and bandwidth that enable high-resolution measurements or high data rates, the 120 GHz industrial, scientific, and medical (ISM) frequency range is extremely appealing for radar and wireless communication applications. Every radar system needs antennas, which are essential components. They affect the system's bandwidth and usable range in addition to being in charge of the spatial radiation. The antennas are frequently mounted on chips [1] or incorporated into various packaging technologies [2] at frequencies greater than 60 GHz. However, methods for designing antennas on printed circuit boards (PCB) over 100 GHz have been developed employing patch antennas [3] and pricey high-frequency composite material. Leaky wave antennas [4–6] are frequently used as feed when substrate integrated waveguide (SIW) constructions are used. When utilizing a leaky wave antenna, the radiating fields are often only focused on one plane unless an array technique is used, which uses many parallel SIW lines. The leaky wave antennas radiate with the Poynting vector approximately in the same plane as the PCB plane.

The objective of this study is to create an appropriate antenna for a stand-alone SIW radar system using 120 GHz PCB technology that is inexpensive. Most previous published antennas often operate at a significantly lower frequency spectrum [7–9], which is the key distinction from our study. Designs requiring substrate cuts or holes in the substrate metallization less than 100 mm are necessary for designs encompassing frequencies up to 90 GHz [10] or even 120 GHz [11], which raises the cost of

Received 17 November 2022, Accepted 11 January 2023, Scheduled 22 January 2023

* Corresponding author: Ahmed Mohamed Montaser (prof.ahmed.montaser@gmail.com).
The author is with the Electrical Engineering Department, Faculty of Technology and Education, Sohag University, Sohag 82524, Egypt.

production. The antenna is built on a very inexpensive Rogers RO4350B substrate and was designed as simple as possible to avoid relying on substrate cutouts, structures smaller than 100 mm [12], or any other configuration that would make the manufacturing process more difficult. This ensures low manufacturing costs and quick prototyping at those very high frequencies.

The integration of Deep Learning (DL) mechanisms into an optimization approach that chooses the optimal antenna parameters and performance is the subject of another field of study. Incorporating an optimizer into the deep learning architecture would speed up the design and optimization process because fewer simulations would be required. Deep learning is a potent estimating or forecasting technique that has the benefit of learning and may deliver precise answers for a particular job. DL attempts to model nonlinear circumstances by using a mathematical representation of the anatomy of the brain. Therefore, the suggested DNN model is a reliable and accurate computation method as opposed to pricey simulation and measurement. Ref. [13] presents a thorough analysis of several research publications that deal with the design and optimization of antennas using deep learning, covering the various methods and algorithms used to create antenna parameters based on required radiation properties and other antenna criteria. Also, a unique modified efficient K-Nearest Neighbors (KNN) technique is shown in [14], and this method, which is regarded as a kind of neural network, has the benefit of requiring fewer samples of training and testing data.

The authors in [15] applied a hybrid DNN system with MGSA-PSO algorithm to design a complex antenna with high radiation characteristics, then an array of 16 antenna elements was designed, and then applying the DNN system to feeding phases for 16 antenna elements, to produce the required beam-steering. In [16], the authors applied very powerful algorithms with DNN system to design a beam forming for a 64 elements Plasmonic Nano antenna array, which led to achieving high-precision beam steering by controlling all antennas, then the authors reduced the number of active antennas to only 5 active antennas to make beam steering, in order to reduce the expensive feed costs, and the DNN system once again managed to get the highest gain and excellent beam steering work by activating only 5 active antennas from the whole array, demonstrating the strength, versatility, and efficiency of the used prediction system. In [17], the authors designed an applicator that contained 35 antennas working with a multi-resonance system. This array was designed with a DNN technique, which greatly contributed to heating all tumors in the breast of different types and volumes.

The authors of [18] synthesized the radiation patterns using a patch antenna array 4×1 with an inter-element spacing of 0.28λ. The radiation pattern served as the input, and the outputs — the amplitude and phase of the antenna elements — were obtained by building a DNN. The suggested DNN has been trained using several radiation model samples that exhibit respectable ability in generating the radiation patterns. Due to the inherent nonlinearities associated with their radiation patterns, antennas are generally considered to be the best possible candidates for DNNs. Neural systems are undeniably common due to their ability to link data with current expert knowledge about issues, as well as their accurate and quick learning and strong generalization capabilities.

In the beginning of this study, we presented a patch antenna construction that would function in the 120 GHz ISM band. Surface-wave suppression, gain performance, and a narrow beam-width radiation pattern are all improved by the introduction of SIW. The comparison of the SIW antenna's measured and simulated results is then displayed. A DNN with a backpropagation approach and a weighted MGSA-PSO algorithm is also used for beam steering of a 20 antenna array operating at 120 GHz by anticipating the appropriate feeding phases. A number of instructive examples are positioned to beam-steer the pattern in the appropriate direction.

The presented paper is organized as follows. In Section 2, the antenna design configuration is presented. In Section 3, the antenna array configuration, a brief introduction to the DL model, and discussion results are explained. Finally, Section 4 concludes the results.

2. ANTENNA DESIGN AND RESULTS

High-frequency circuit design is a perfect fit for SIW technology [19]. The location of the vias and the substrate's material qualities are the sole factors that affect the electric characteristics. Therefore, it is not essential to use expensive PCB manufacturing techniques to obtain extremely small structures, which are typically required in high-frequency design. One double-sided metallized RO4350B high-

frequency substrate serves as the design's foundation. The substrate's height is set at 0.254 mm. This substrate's key benefit is that it is less expensive than other high-frequency substrates.

Geometrical configuration of the proposed circularly polarized SIW cavity-backed leafed-slot antenna is shown in Fig. 1. Its circular backed cavity is constructed by vias' arrays on a single substrate; the electromagnetic fields are radiated through the dielectric aperture of the SIW circular cavity. The exact placement of via can be used for matching purposes if the antenna design fields of the cavity and slotted patch are compatible. The SIW circular cavity greatly affects the current distribution within the antenna parts, which greatly affects the directivity and reflection coefficient of the antenna. The proposed antenna is implemented on a single layer substrate which provides high radiation efficiency with enhanced impedance bandwidth. Most designs are based on a single double-sided metallized RO4350B high-frequency substrate, and to eliminate the spurious radiation, the height of the substrate is chosen at 0.254 mm. A leaf slot is etched on a concave sides rectangular patch of length L_6 and width W_7 which are printed on the bottom surface of the substrate layer, while the distance between partial ground plane and the patch of a rectangle with concave sides is g, and by adjusting the distance g, the amount of coupling between two resonators can be controlled. An inset feed port microstrip line with width of W_2 is used to excite the SIW cavity and radiated patch antenna. This patch content's x slot enhances radiation efficiency. Through both the leaf slot in the concave rectangle at the ground plane and the x slot in the top patch, the surface current distribution inside this antenna is controlled. The optimized leaf slot in the surface of the concave rectangular patch responds to circular polarization antenna and improves impedance bandwidth. Based on above discussion, the microstrip patch is excited at dominant mode through proximity effect by the SIW cavity. As a result, two resonators working at their fundamental modes radiate electromagnetic fields. By a proper choice of resonators dimensions,

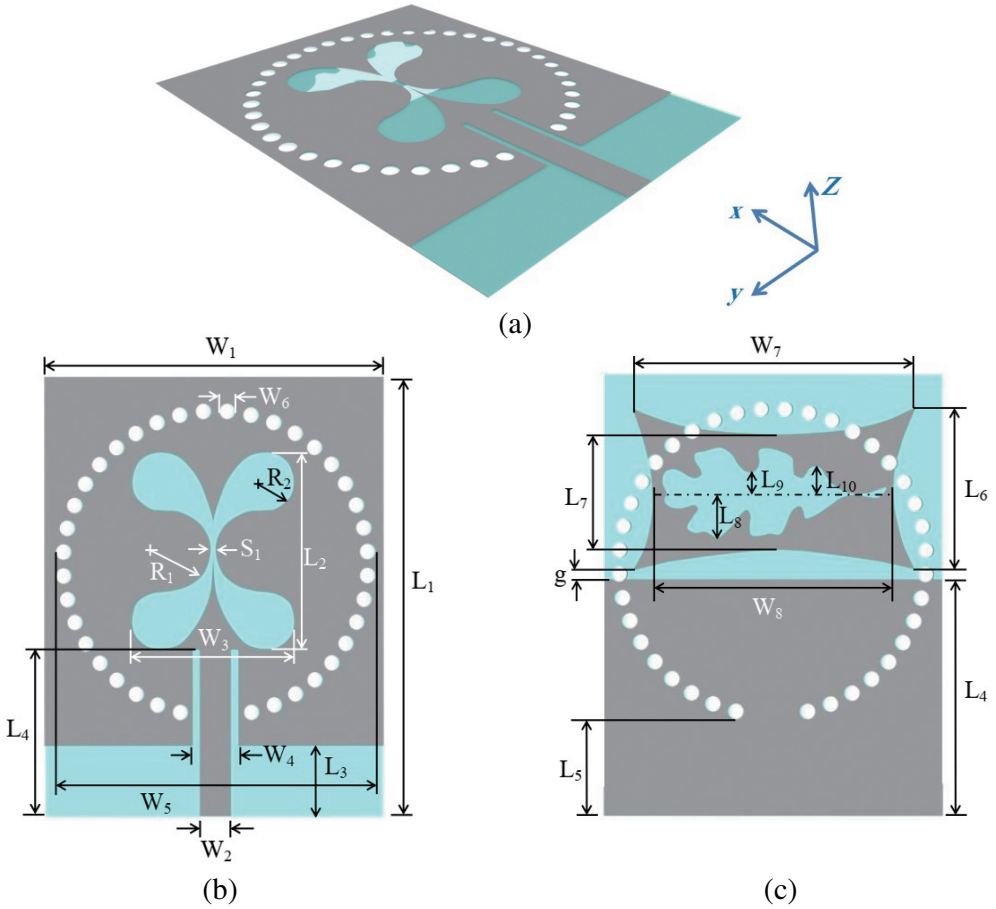

Figure 1. Proposed antenna structure. (a) 3D view. (b) Top view, and (c) Back view.

resonant frequencies of the cavity and patch are merged, and wide bandwidth is achieved.

The MGSA-PSO algorithm [20, 21] was used to optimize the proposed antenna's top patch, partial ground plane, and the leaf slot etched on concave sides rectangular patch such that it would resonate at 120 GHz with good gain, efficiency, and an Axial Ratio (AR) of less than 3 dB. Utilizing Computer Simulation Technology (CST)-Microwave Studio (MWS) [22], the antenna is fully modelled, and its dimensions are optimized using a MATLAB-coded optimization technique. The improved antenna will also be modeled using MATLAB code with the finite difference time domain (FDTD) computational approach to evaluate the results. The goal function shown below is taken into account in this situation to optimize antenna gain (G) and radiation efficiency (e) while minimizing return loss (S_{11}), AR, and side lobe level (SLL) at the operational frequency range.

$$\mathrm{Obj}_1 = [\min\{S_{11}(f) + \mathrm{AR}(f) + |\mathrm{SLL}|_{\mathrm{dB}}\} + \max\{G(f) + e(f)\}]_f = 120\,\mathrm{GHz} \tag{1}$$

A circularly polarized antenna that is matched at 120 GHz and has a good gain and high efficiency can be produced by optimizing the antenna's dimensions. The best calculated values of the optimized antenna dimensions are shown in Table 1 together with the choice space for the variables.

Table 1. The initial and optimized dimensions for proposed antenna. (all units in millimeter).

Variable	initial Value	Decision space		Best value
		from	to	
W_1	3.5	2.5	4.5	3.85
W_2	0.3	0.25	0.5	0.35
W_3	1.5	1	2	1.91
W_4	0.45	0.3	0.7	0.52
W_5	3	2	4	3.68
W_6	0.2	0.15	0.25	0.19
W_7	3	2.5	4	3.18
W_8	2.5	2	3.5	2.71
L_1	4.5	3.5	5.5	5.01
L_2	2	1.5	3	2.24
L_3	0.75	0.5	1	0.83
L_4	1.5	1	2	1.92
L_5	1.25	0.5	1.5	1.09
L_6	2	1.5	2.5	1.85
L_7	1	0.75	1.5	1.3
L_8	0.4	0.1	0.75	0.51
L_9	0.4	0.1	0.75	0.28
L_{10}	0.4	0.1	0.75	0.31
R_1	0.35	0.3	0.75	0.51
R_2	0.35	0.3	0.75	0.42
S_1	0.75	0.5	0.2	0. 98
g	0.3	0.1	0.9	0.13

The simulated and measured proposed antenna characteristics are shown in Fig. 2. The simulated and measured free-space reflection coefficients at 120 GHz are presented in Fig. 2(a) for antenna design. The simulation was designed for the proposed antenna in two techniques, the first using the Computer Simulation Technology (CST) Microwave Studio package and the second using the FDTD method written with MATLAB code, to confirm the results. A rotating stage and a vector network analyzer

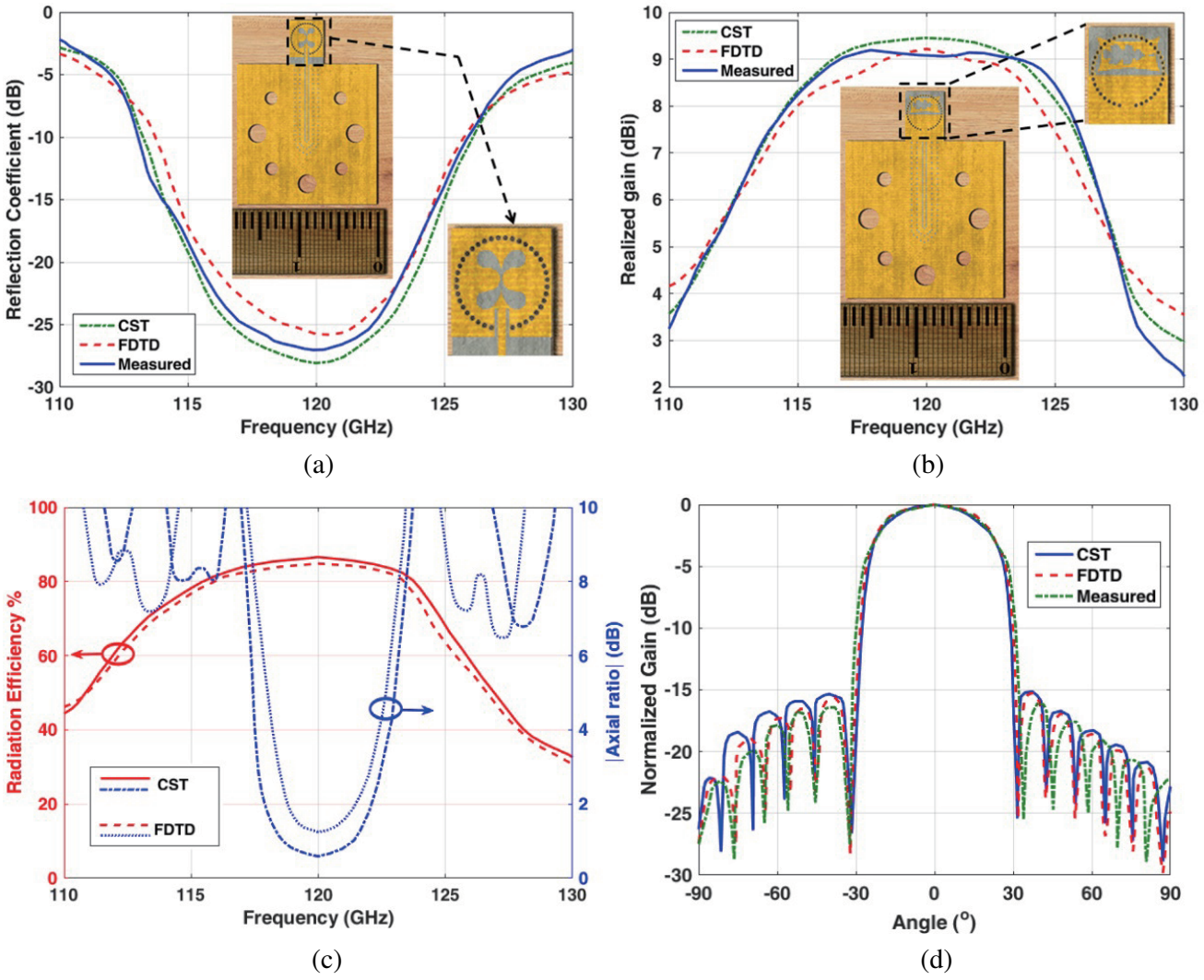

Figure 2. Proposed antenna radiation characteristics. (a) Reflection coefficient. (b) Realized gain. (c) Radiation efficiency and axial ratio, and (d) Radiation pattern in X-Y plane.

(VNA) are used to characterize the antenna. A transition from rectangular waveguide (WR-06) to SIW is required to link the antenna to the VNA. A single slot is drilled into the copper of the SIW line to enable coupling from a rectangular waveguide onto the substrate due to the high frequency and therefore very compact structures. The rectangular waveguide's flange may be attached to the SIW line using proper drills, which are provided. The simulations run with the transition and the measured reflection coefficients agree. The dimensions of the slot, which are susceptible to production tolerances, have a significant impact on the frequency behavior of this transition. However, the ISM band's frequency range of 110 to 130 GHz is well covered by the measurements, and the antenna displays acceptable matching. Photographs of the fabricated antenna inserts are shown in Figs. 2(a) and (b). By comparing the simulation with measured results, there was a good agreement between measured results and both the simulation results obtained from the CST package and FDTD method over a wide frequency range. It is crucial to stress that switching from a rectangular waveguide to a SIW is solely used for component characterization and is not necessary for the final system.

Figure 2(b) shows the comparison between simulated and measured realized gains, and it can be noticed that the measured gain is in good agreement with the numerical results. The measured realized gain for antenna is close to the simulated value of 7.52 dBi at 120 GHz. As for the antenna

radiation efficiency, it has exceeded 86% at 120 GHz, and this percentage is very excellent in this range of frequencies. Full responsibility for the amount of high efficiency is the metallization area in the upper patch and the x slot engraved in it. It can be observed that the absolute axial ratio has exceeded 3 dB from 117.6 to 122.5 GHz, which makes the antenna work with circular polarity in this range; the part responsible for the axial ratio characteristic is the leaf slot in the concave rectangle because the current distribution on the edges of this leaf is constantly changing. The proposed antenna efficiency and axial ratio are shown in Fig. 2(c).

Figure 2(d) shows normalized radiation pattern for the proposed antenna. It can be observed that this antenna has narrow band end-fire radiation pattern, and the Half Power Beamwidth (HPBW) is 46°, which makes the proposed antenna very suitable for the purposes of radar applications, often requiring a narrow beamwidth with high radiation power and gain to accurately detect objects in high resolution details from long distances. The measured results of the radiation pattern are consistent with the simulations and show the desired radiation behavior over the whole operating frequency range. The antenna provides low side lobe levels in the directional plane.

3. ANTENNA ARRAY CONFIGURATION AND DEEP LEARNING

An antenna array is a setup of separate radiating components that are placed in space and have the ability to generate directional radiation patterns. Let's assume that there are antenna radiators positioned symmetrically along the y-axis for a linear antenna array, as illustrated in Fig. 3. The array consists of 20 circularly polarized elements of the optimized antenna operating at 120 GHz. With an identical distance of 1 mm between any two succeeding elements, the elements are evenly dispersed in a linear design. The suggested antenna array is constructed to combine the various beam patterns. By altering the phase of the input signal allotted to each antenna element, the radiation pattern may be guided in the desired direction with a high gain and a side-lobe level as low as feasible. The feeding stages of DNN learning are therefore thought to be optimized by the MGSA-PSO algorithm.

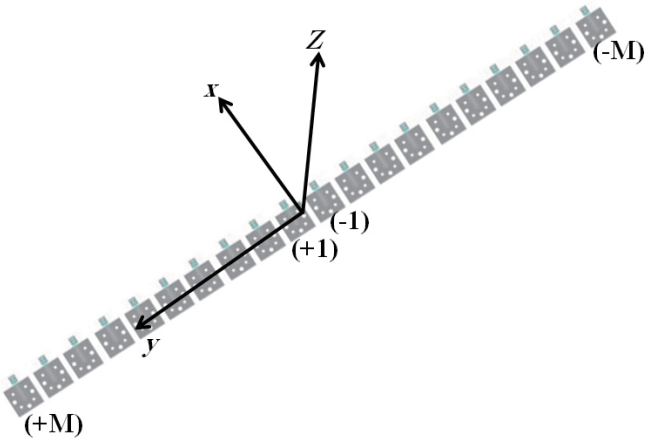

Figure 3. 3D view of antenna array structure.

DL is a subclass of artificial intelligence (AI) that is simply a neural network having three or maybe more layers [13]. DL neural networks are made up of several layers of connection weights, with each layer improving and perfecting the forecast or classification. The movement of computations through the network is referred to as forward propagation. The input and output layers of a deep neural network are the steps that are visible. The final prediction or classification is carried out by the deep learning model in the output layer after the data has been processed in the input layer. When a model is trained, a technique called backpropagation is used to modify the weights of the function by iteratively traveling back through the layers and using tools like gradient descent to produce prediction errors. A neural network may make predictions and correct any errors by using a combination of forward propagation and backpropagation. Over time, the algorithm becomes more accurate.

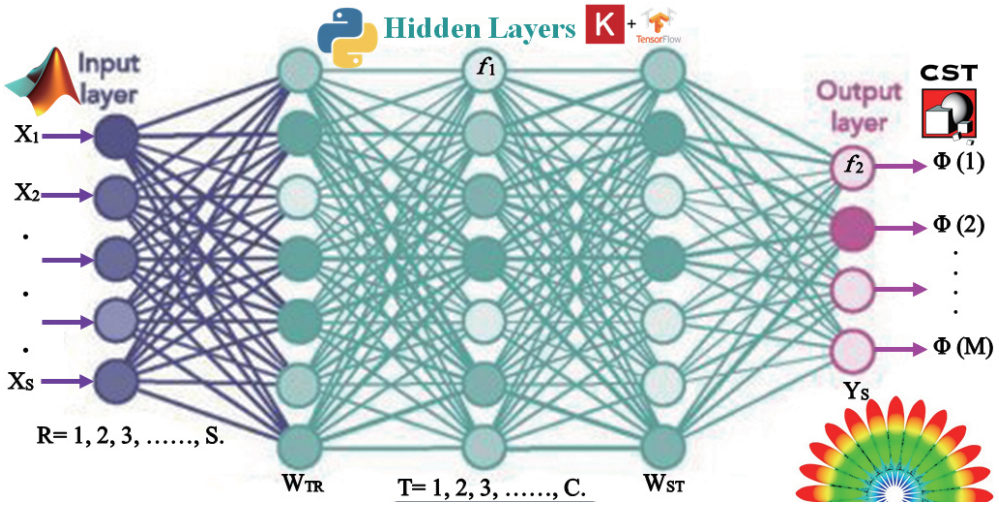

Figure 4. The neural beam-former architecture.

For beam-steering, DL is used in this study on a 120 GHz antenna array. With a thorough examination of the NN's structure as shown in Fig. 4, Tensorflow and Keras framework [23] are utilized to build the model, while Python version 3.8 is used to implement the DNN technique. Our research reveals that it is made up of several layers, including an input layer, which is thought of as a foundation for information, an output layer, and hidden inner layers, which seem to be layers with changeable reconfiguration. The neurons in one layer of the network do not share information with one another since each layer has a distinct structure and function. These networks need supervised learning, but the Multilayer Perceptron (MLP) network may be fed by one hidden layer. In this hidden layer, each MLP node has a specific purpose. The input vector's dimension [24] is the same as the number of nodes, S, where T is the index of the hidden layer, and R is the index of the input layer with $R = 1, 2, \ldots, S$. $B = 1, 2, \ldots, Z$ is the index of the output layer.

The smallest error between the neural model output y_B and the training data $Data_B$ is used to determine the interconnect weights. The training procedure's objective is to optimize the network connection weights ω_{rt} and ω_{bt} in order to reduce the error function Error(g), which is defined as:

$$\text{Error}\,(g) = \frac{1}{2}\sum_{B=1}^{Z}\sum_{T=1}^{C}\sum_{R=1}^{S}\left[y_B\left(x_r,\omega_{rt},\omega_{bt}\right) - \text{Data}_B\right]^2 \tag{2}$$

where $G = 1, 2, \ldots, g$ is the index of the training set. The DNN is trained on a finite training set of G, forming the input vectors $\{G = 1, 2, \ldots, 20\}$, where $G \in [500, 12000]$, to learn the input output relationship [25]. Clearly, if we set the selection probability of some datapoints, then, we reduce the size of the training set by eliminating these datapoints from the batch selection, batch size = 128. A smaller training set is typically easier to fit but also to over-fit. Generally, the quantity of training samples sent to the DNN networks is known as the batch size. One or more batches can be created from a training dataset. The learning algorithm is known as batch gradient descent when all training examples are supplied in a single batch. The learning algorithm is known as stochastic gradient descent when the batch size is one. The learning algorithm is known as mini-batch gradient descent when the batch size is greater than one and lower than the training size. It is more common to use 32, 64, and 128 batch sizes in mini-batch gradient descent. The larger batches increase network accuracy.

A small amount of deviation from the goal outcome is necessary for DNN training. In this work, a mini-batch gradient descent based technique is employed to accomplish this training. The system created here has 20 output neurons and 22 input neurons to address this issue. The training parameters are listed in Table 2.

From the previous table, the quantity of epochs indicates how many times the training dataset has been traversed. Every epoch suggests that the training sample has the ability to update the internal model parameters. One or more batches might be present. It is possible for there to be zero or infinitely

Table 2. Training parameters of DNN.

Parameter	Value
Training Data	75%
Testing Data	15%
Evaluating Data	10%
Input Neuron	22
Hidden layer	3
Hidden Neuron	36
Output Neuron	20
Epochs	12000
Coefficient of training	0.04
The activation function at the hidden nodes f_1	Sigmoid tan
The activation function at the output nodes f_2	Sigmoid tan

many epochs. In most cases, hundreds or thousands of epochs are picked. This enables the network to sufficiently lower the error. A developer must look at the learning curves of error and accuracy to select the best epoch value. These curves can be used to identify whether the model has learnt too much, too little, or is well prepared for training.

Figure 5(a) represents the training, validation, and testing performance of the proposed neural networks structure. The performance plot of the neural network is shown in Fig. 5(b), and the gradient at 12000 epoch is 5.61×10^{-5}. One of the most crucial factors utilized to fine-tune the models is learning rate. It updates network weights to reduce error. Model performance would suffer if the learning rate was set too low or too high. A low learning rate will result in little network weight updates and slow down training, whereas a high learning rate will result in divergent error behavior. In actual training, a high learning rate should be used at first since random weights at the beginning are far from ideal and learning rates will fine-tune the network weights by lowering their value during training. The learning process may begin with a large value, such as 0.1, and move on to smaller values, such as 0.01, 0.001, etc. For each iteration, the weights ω_{rt} and ω_{bt} are modified by:

$$\Delta\omega_v = -\eta \frac{\partial \text{Error}}{\partial \omega_v} \tag{3}$$

Sector-width intervals of 10° were employed in the training set for each scenario, where the ω_v stands for the output layer weights. The mean square error performance of the MLP Network is shown in Fig. 6.

The capability of generalization is one of neural networks' major benefits. Accordingly, a trained network will categorize new data in the same category as the learning data, as if it has never encountered it before. Only a small portion of all imaginable neural network patterns are available to developers in the majority of real-world applications. The dataset should be divided into three parts for the optimal generalization:

- The training set is used to train a neural network: The dataset's error is reduced throughout training.
- A neural network's performance on patterns that were not taught during the learning phase is assessed using the validation set.
- A test set for assessing a neural network's general effectiveness.

The two most significant activities in this situation are network architecture and network testing (generalization). In order to create a network, input vectors x_g, where $g = 1, 2, \ldots, 20$ are initially

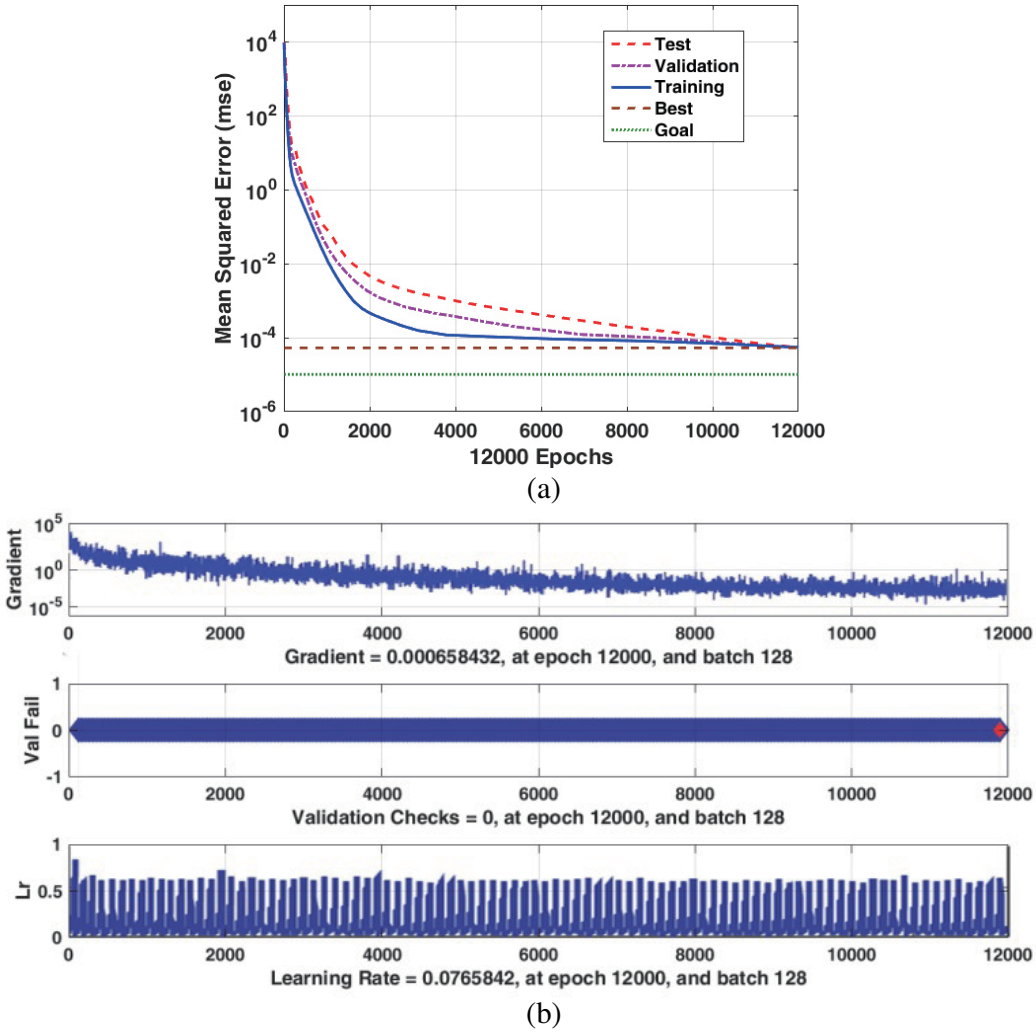

Figure 5. Neural networks results. (a) Validation and training performance of DNN. (b) Performance plot of the neural network.

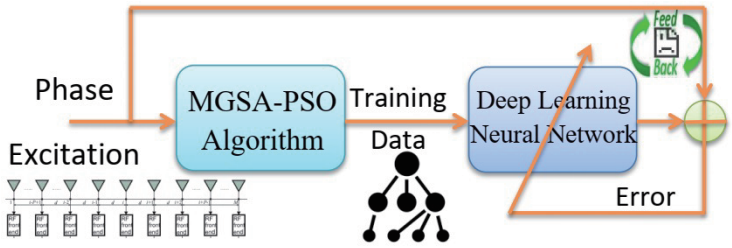

Figure 6. Neural network training procedure.

formed. Next, input/output pairs $\{x_g, \varphi_q\}$, where $q = 1, 2, \ldots, 22$, are generated. We create x'_g vectors for the testing input samples while testing a network and then provide the neural networks the input vectors x'_g. Finally, the output of the network is discovered. The number of hidden neurons selected depends heavily on the characteristics of the nonlinearity that must be replicated. As listed in Table 2, 36 hidden neurons in this investigation provided evidence that the procedure was convergent, and the neural model produced was accurate. Hidden neurons are the number of neurons in the hidden layer.

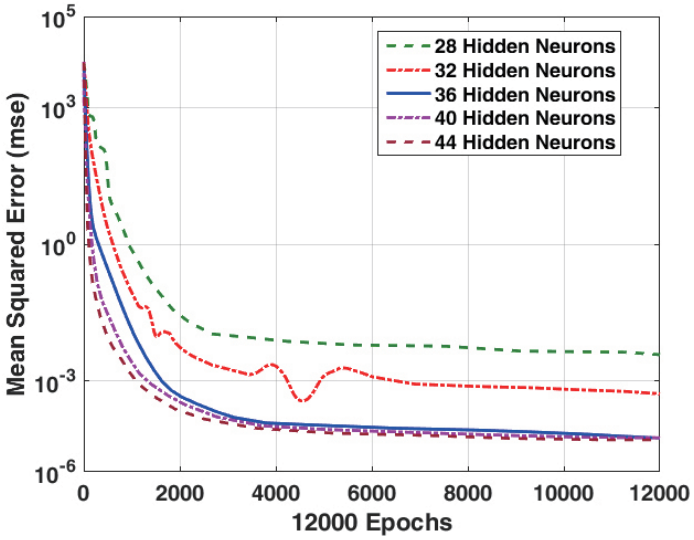

Figure 7. Training curves in terms of the mean square errors (MSE) for different neural networks with varying hidden neurons.

Because it affects the performance of the DNN model, choosing the optimal number of neurons for the hidden layer is crucial. To choose a proper NN topology, five networks with different numbers of hidden neurons (28, 32, 36, 40, and 44 neurons) are studied. The training curves in terms of the mean square errors are shown in Fig. 7. It can be noticed that when the neural networks are used, if the number of their hidden neurons is equal to 28 or 32, the mean square error (MSE) values will be equal to 3.75×10^{-3} and 5.18×10^{-4}, respectively. The MSE in these two cases cannot converge to the lowest value, which indicates that these two DNN networks are not accurate enough to use and predict the output. Generally, under-fitting will result in large training errors when there are not enough hidden neurons, as clear in cases 28 and 32. As for the remaining three cases (36, 40, and 44 neurons), the MSE is almost the same, which is equal to 5.61×10^{-5}, which indicates that this network should be more accurate to be used to predict the correct directions. Low training errors will be the result of over-fitting if there are too many hidden neurons. It will unnecessarily slow down the training and frequently lead to poor generalization. As long as the last three cases have almost the same result, the DNN network that has the least number of neurons is chosen (36 neurons), so that it has ease in calculations, computational facility, and is not time-consuming. Finally, the quantity of input training instances determines the size of the hidden neurons.

The neuron used in this network is the continuous nonlinear neuron, whose activation functions f_1 and f_2 are tan sigmoid functions [26]. Divide the area into 40 sectors and repeat every 4 degrees between -80° and 80° degrees inclusively to investigate the ideas discussed in the previous section. By adding more element arrays, one may create more precise space division sectors. The neural network's input vector is a 40-bit binary code (one bit for each sector). A source in the sector with a bin input of (+1) is precisely on (main lobe). Then convergence might be accomplished more quickly.

The following examples demonstrate how the suggested method, as illustrated in Fig. 6, has been fully evaluated. The excitation voltages were tuned with equal amplitudes and varying phases to synthesize the 20-element antenna array [27]. The anticipated simulation results for the reference antenna must show radiation patterns with low SLL and large lobes pointing in the general direction of important signal. The database holds all the data (input/output) generated during simulation using the MGSA-PSO algorithm, and the application specifies the required radiation pattern between -80° and 80°. The proposed antenna array is analyzed using CST-MWS and linked with MGSA-PSO algorithm, Matlab-coded, to optimize the antenna array phases. In order to accomplish the target, the objective function listed below is used. This objective function optimized the 17 required orientations of the antenna array from -80° to 80° as training data for the DL technique.

$$\text{Obj}_2 = \max |E_t(\theta_i, \phi_i)| + \min(|\text{SLL}|_{\text{dB}}) \tag{4}$$

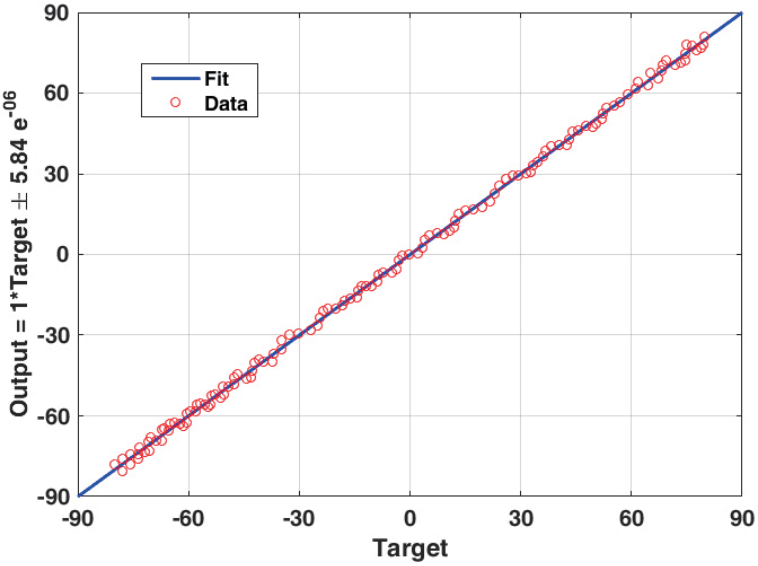

Figure 8. Training state of the network created during training.

Figure 8 displays the regression's visual result. The objectives are lined up with the network outputs as open circles. Perfect alignment and best linear fit are depicted by the solid line (output equal to the targets). The DNN model with five layers was trained to provide the beam steering for phase feeding for each antenna element in accordance with the relationship between the input and the target. A 75% from available data are employed for training process while 25% from available data are used for validation and testing process in the DNN model. The DNN model has calculated the average percentage errors (APEs) for the beam-steering direction using the following equation:

$$\text{APE} = \frac{\sum \left| \frac{\phi_{Truth} - \phi_{\text{Pred}}}{\phi_{Truth}} \right| \times 100}{\text{Total number of Scenarios}}\% \tag{5}$$

where ϕ_{Truth} is the desired beam-steering direction that can be achieved by assigning the optimal phases. The suggested deep-learning technique is used to determine the optimal phases, which beam-steers the pattern in the direction ϕ_{Pred}, and the total number of scenarios is the total number of trained or tested scenarios according to the kind of computed APE.

The DNN model has calculated the average percentage errors (APE) for the steering directions, as shown in Fig. 9. It is obvious that for every deep learning application, the number of training points assigned has an impact on the APE value. In contrast, increasing the number of training points enhances the system's accuracy, and vice versa. The scatter diagrams of the ground truth and prediction angle steering directions results for the training and testing datasets are displayed in Fig. 10 in order to visually understand the correlations between the results. A suitable APE of 0.253% was acquired as for the training data, and an appropriate APE of 0.279% was obtained as for the testing data based on Fig. 9, which shows the topology of calculating the APE for DNN model. It is obvious that the points will follow a linear pattern, indicating that the results have a strong linear association.

The 17 desired orientations of the linear array with $N = 20$ elements were carried out to show the efficacy of the technique described in the preceding section for guiding single beams in the desired direction by managing the phase feeding of each array element. The numerical results are demonstrated that NNs using the MGSA-PSO algorithm have exceptional phase control capabilities for beam pattern generation in a variety of circumstances as shown in Fig. 11. To validate the results of the MGSA-PSO algorithm for antenna array, one run of the training results (in the case that the desired angle is 0°) was compared with FDTD method design for the same case as shown in Fig. 12. It can be noticed that the results are completely compatible between the trainings with the MGSA-PSO algorithm and the FDTD method.

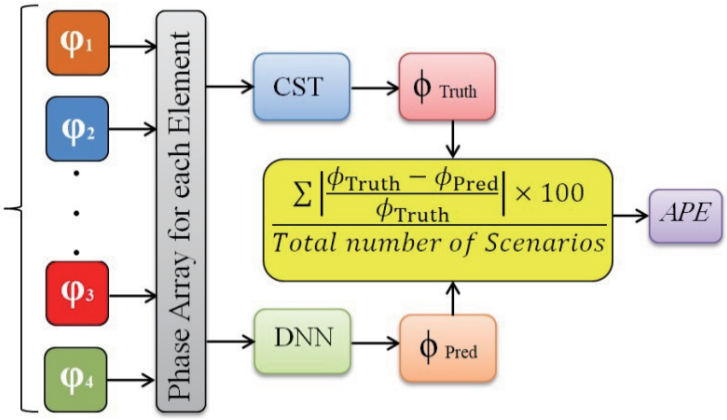

Figure 9. The topology of the calculating APE.

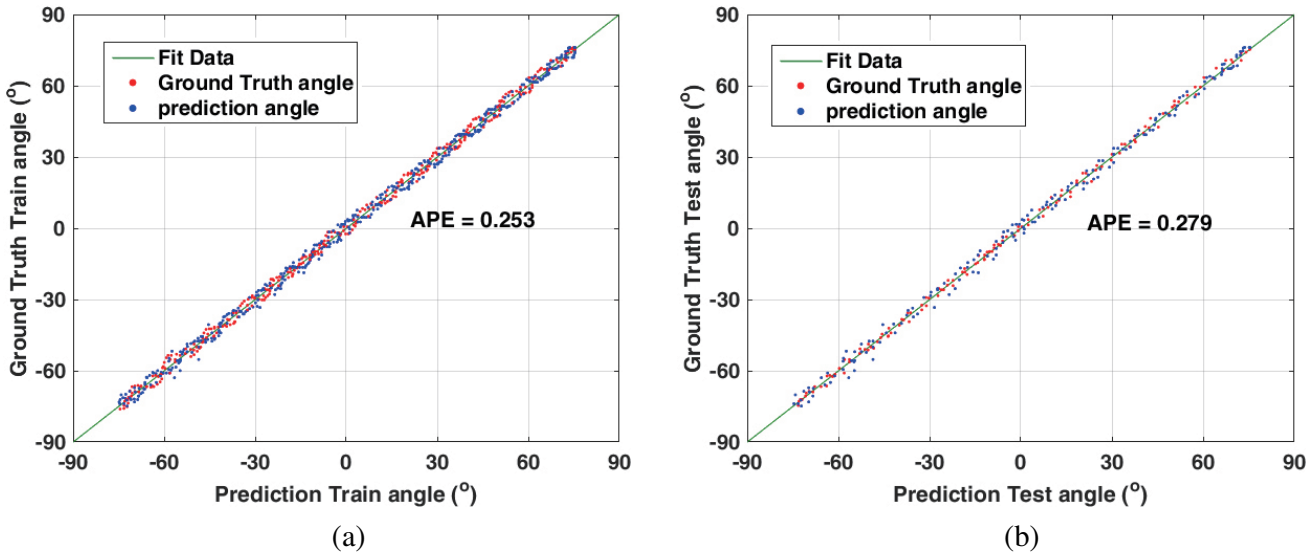

Figure 10. Scatter diagrams of the ground truth and prediction angle steering directions by the DNN model for (a) Training data. (b) Test data.

After the training phase, it is crucial to test the neural network on a database that was not utilized for learning. This test enables both the evaluation of neural system performance and the identification of problematic data types. In the event that the performance (distinctive characteristics or representativeness of each data class) is subpar, it will either update the network architecture or modify the learning base.

In order to evaluate the suggested approach for the synthesis of a linear array, several simulation scenarios are investigated at $\varphi = -73°$, $-22°$, $38°$, and $66°$. The simulated results for the built-in antenna array setup with 20 elements at 120 GHz using the DNN technique are displayed in Fig. 13. The outcomes show that the synthesized and intended requirements are very closely related. This demonstrates the effectiveness of the suggested action. The DNN provides the best solutions for situations where nonlinear modeling of complex data needs to be simulated because of its better learning, generalization, parallel computing, and error tolerance qualities. To more clearly demonstrate the benefits of our DNN model, we compare the conventional method (such as MIMO phased array using Complete Wave Simulations using CST) and our DNN predicted technique in terms of realized gain, SLL, axial ratio, HPBW, radiation efficiency, time-consuming, iterations of computation in CST, the difference between computed radiation and target radiation, and finally accuracy rate. This comparison

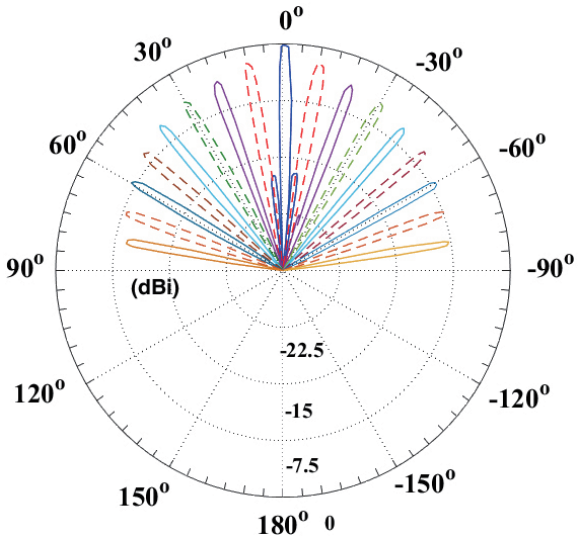

Figure 11. Radiation pattern of 20 elements antenna array optimized using MGSA-PSO with respect to minimum SLL.

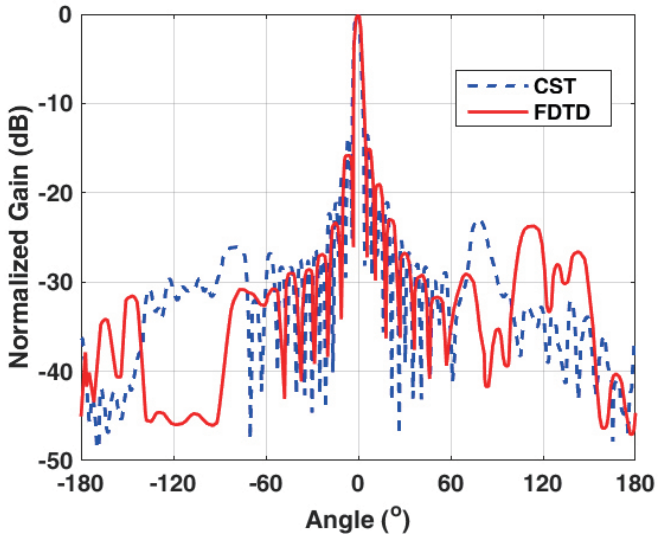

Figure 12. Validate the result of the MGSA-PSO algorithm with FDTD method for antenna array.

is performed for four test scenarios at angles $\varphi = -73°$, $-22°$, $38°$, and $66°$. Our DNN model technique has achieved a remarkable superiority over the conventional method (MIMO) in terms of realized gain, radiation efficiency, SLL, axial ratio, and HPBW, and generates results about 544.4 times faster than the traditional one. As can be seen, this is due to the many iterations the MGSA-PSO algorithm does. We also calculate the discrepancy between estimated radiation and target radiation, which indicates the accuracy rate of the radiation outcomes. In particular, the accuracy rate for the top 12% of samples might go over. In reality, as deep learning models can only generate probabilistic predictions, they may not be exact enough to achieve 100% accuracy, necessitating extra optimization procedures. From the above, it can be concluded that the DNN model is better than the conventional method, either from the aspect of computational iterations and quantities, time consumption, or result accuracy rate. Consequently, the outcomes validate the DNN model, and it offers an effective method in a variety of application environments; the comparison is listed in Table 3. A DNN, which can be trained to deal with any number of elements, separation, and excitation, is used in this technique. Once the network has been trained, the parameters with regard to the input may be discovered.

Table 3. Phase array comparison between conventional method (MIMO) and our DNN predicted.

Items	Test no. 1 Desired angle −37°		Test no. 2 Desired angle −22°		Test no. 3 Desired angle 38°		Test no. 4 Desired angle 66°	
	MIMO	DNN	MIMO	DNN	MIMO	DNN	MIMO	DNN
Realized gain (dBi)	16.9	19.5	17.5	20.4	17.3	20.1	17.1	19.8
Radiation Efficiency %	71.3	80.9	75.6	84.8	74.5	82.1	73.4	81.5
SLL (dB)	−8	−14	−11	−19	−10	−17	−9	−15
|Axial ratio| (dB)	3.2	2.8	1.8	1.5	2.3	1.9	2.9	2.4
HPBW (°)	35.2	9.1	30.7	7.5	33.6	8.4	34.5	8.8
Time-consuming (min)	937	2.1	980	1.8	915	2.3	955	1.9
Iterations of computation	463	1	491	1	458	1	432	1
The difference between computed radiation and target radiation (°)	9.4	0.8	5.1	0.4	6.8	0.7	8.3	0.5
Accuracy rate %	79	91	84	95	82	93	80	92

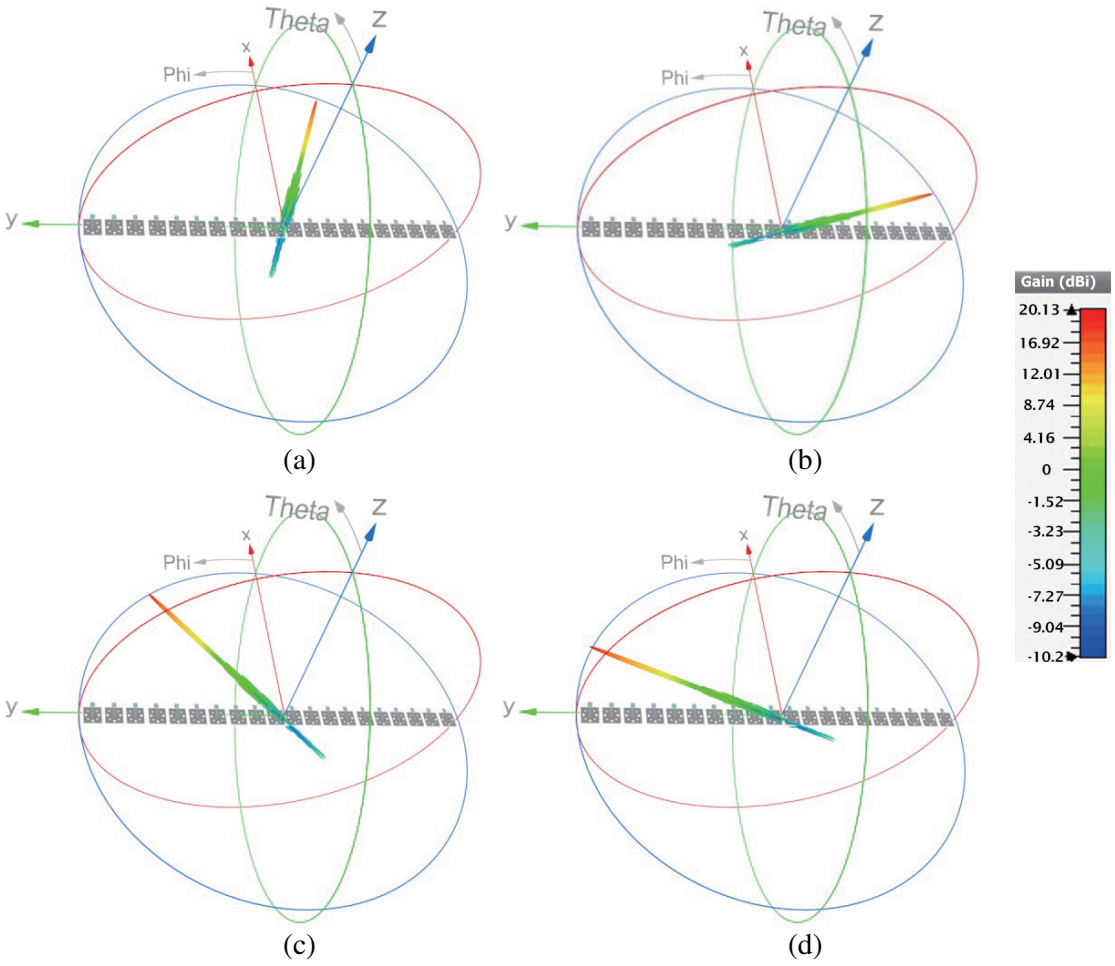

Figure 13. 3D Radiation pattern of several tested scenarios. (a) Beam steering at angle −73°. (b) Beam steering at angle −22°. (c) Beam steering at angle 38°, and (d) Beam steering at angle 66°.

4. CONCLUSION

This paper presents a compact, inexpensive SIW antenna for the 120 GHz ISM band. One RO4350B laminate is used to build the antenna. A realized gain around 7.52 dBi was measured for the proposed antenna and HPBW for main loop around 46°. This makes the proposed antenna very suitable for the purposes of radar applications, often requiring a narrow beam width with high radiation power and gain to accurately detect objects in high resolution details from long distances. The measured radiation pattern and computational results are in excellent agreement and demonstrate good concentration for a one element antenna. Furthermore, a 20 antenna element array working at 120 GHz has been used to beam-steering approach. The antenna array's radiation pattern is beam-steered using the DNN model. Results indicate that the required and synthesized specifications are in accord. Compared to the conventional method, our DNN model achieved a remarkable superiority in terms of realized gain, SLL, axial ratio, HPBW, radiation efficiency, iterations of computation, accuracy rate, and savings in processing time. This technique utilizes a neural network that may be trained for any element count, spacing, or excitation. The network can determine the parameters with regard to the input once it has been trained.

ACKNOWLEDGMENT

The authors would like to express their gratitude to the National Telecommunication Regulatory Authority (NTRA), Ministry of Communication and Information Technology in Egypt for their support.

REFERENCES

1. Ng, H. J. and D. Kissinger, "Highly miniaturized 120-GHz SIMO and MIMO Radar sensor with on-chip folded dipole antennas for range and angular measurements," *IEEE Trans. on Microw. Theory and Tech.*, Vol. 66, No. 6, 2592–2603, 2018, DOI: 10.1109/TMTT.2018.2829178.
2. Beer, S., H. Gulan, C. Rusch, et al., "Coplanar 122-GHz antenna array with air cavity reflector for integration in plastic packages," *IEEE Antennas and Wireless Propag. Lett.*, Vol. 11, 160–163, 2012, DOI: 10.1109/LAWP.2012.2186783.
3. Hasan, R., W. A. Ahmad, J. H. Lu, et al., "Design and characterization of a differential microstrip patch antenna array at 122 GHz," *IEEE Radio and Wireless Symp. (RWS)*, 28–30, 2018, DOI: 10.1109/RWS.2018.8304937.
4. Ouseph, L., A. Mathews, and A. Chandroth, "Substrate integrated waveguide without metallized wall posts," *Progress In Electromagnetics Research Letters*, Vol. 77, 7–14, 2018, doi:10.2528/PIERL18041806.
5. Ismail, N., et al., "Wideband substrate-integrated-waveguide BPF incorporated with complimentary-split-ring-resonators," *2018 Progress In Electromagnetics Research Symposium (PIERS — Toyama)*, Japan, August 1–4, 2018.
6. Huang, Y., Z. Shao, and L. Liu, "A substrate integrated waveguide bandpass filter using novel defected ground structure shape," *Progress In Electromagnetics Research*, Vol. 135, 201–213, 2013.
7. Kazemi, R., E. Fathy, and R. A. Sadeghzadeh, "Dielectric rod antenna array with substrate integrated waveguide planar feed network for wideband applications," *IEEE Trans. on Antennas and Propag.*, Vol. 60, 1312–1319, 2012, DOI: 10.1109/TAP.2011.2182489.
8. Puskely, J., J. Lacik, Z. Raida, et al., "High-gain dielectricloaded Vivaldi antenna for Ka-band applications," *IEEE Antennas and Wireless Propag. Lett.*, Vol. 15, 2004–2007, 2016, DOI: 10.1109/LAWP.2016.2550658.
9. Hesari, S. S. and J. Bornemann, "Wideband circularly polarized substrate integrated waveguide endfire antenna system with high gain," *IEEE Antennas and Wireless Propag. Lett.*, Vol. 16, 2262–2265, 2017, DOI: 10.1109/LAWP.2017.2713720.
10. Mirbeik-Sabzevari, A., S. Li, E. Garay, et al., "W-band micromachined antipodal vivaldi antenna using SIW and CPW structures," *IEEE Trans. on Antennas and Propag.*, Vol. 66, No. 11, 6352–6357, 2018, DOI: 10.1109/TAP.2018.2863098.

11. Taringou, F., D. Dousset, J. Bornemann, et al., "Broadband CPW feed for millimeter-wave SIW-based antipodal linearly tapered slot antennas," *IEEE Trans. on Antennas and Propag.*, Vol. 61, No. 4, 1756–1762, 2013, DOI: 10.1109/TAP.2012.2232270.
12. Frank, M., F. Lurz, R. Weigel, et al., "Compact low-cost substrate integrated waveguide fed antenna for 122 GHz radar applications," *Int. J. of Microw. and Wireless Technol.*, Vol. 11, 408–412, 2019, https://doi.org/10.1017/S1759078719000072.
13. Misilmani, H. M. E., T. Naous, and S. K. A. Khatib, "A review on the design and optimization of antennas using machine learning algorithms and techniques," *Int. J. RF Microw. Comput. — Aided Eng.*, Vol. 30, No. 10, 1–28, 2020, https://doi.org/10.1002/mmce.22356.
14. Cui, L., Y. Zhang, R. Zhang, et al., "A modified efficient KNN method for antenna optimization and design," *IEEE Trans. Antennas Propag.*, Vol. 68, No. 10, 6858–6866, 2020, DOI: 10.1109/TAP.2020.3001743.
15. Montaser, A. M. and K. R. Mahmoud, "Deep learning based antenna design and beam-steering capabilities for millimeter-wave applications," *IEEE Access*, Vol. 9, 145583–145591, 2021, DOI: 10.1109/ACCESS.2021.3123219.
16. Mahmoud, K. R. and A. M. Montaser, "Machine-learning-based beam steering in a hybrid plasmonic nano-antenna array," *J. of the Opt. Soc. of Amer. B.*, Vol. 39, No. 8, 2149–2163, 2022, https://doi.org/10.1364/JOSAB.458574.
17. Mahmoud, K. R. and A. M. Montaser, "Design of multi-resonance flexible antenna array applicator for breast cancer hyperthermia treatment," *IEEE Access*, Vol. 10, 93338–93352, 2022, DOI: 10.1109/ACCESS.2022.3203431.
18. Kim, J. H. and S. W. Choi, "A deep learning-based approach for radiation pattern synthesis of an array antenna," *IEEE Access*, Vol. 8, 226059–226063, 2020, DOI: 10.1109/ACCESS.2020.3045464.
19. Bozzi, M., A. Georgiadis, and K. Wu, "Review of substrate-integrated waveguide circuits and antennas," *IET Microw. Antennas and Propag.*, Vol. 5, No. 8, 909–920, 2011, DOI: 10.1049/iet-map.2010.0463.
20. Mahmoud, K. R. and A. M. Montaser, "Performance of tri-band multipolarized array antenna for 5G mobile base station adopting polarization and directivity control," *IEEE Access*, Vol. 6, 8682–8694, 2018, DOI: 10.1109/ACCESS.2018.2805802.
21. Mahmoud, K. R. and A. M. Montaser, "Synthesis of multi-polarised upside conical frustum array antenna for 5G mm-Wave base station at 28/38 GHz," *IET Microw., Antennas Propag.*, Vol. 12, No. 9, 1559–1569, 2018, https://doi.org/10.1049/iet-map.2017.1138.
22. Computer Simulation Technology Microwave Studio (CST MWS), Accessed: 2022, [Online], Available: https://www.3ds.com/productsservices/simulia/products/cst-studio-suite/.
23. Chollet, F., et al., Keras. Accessed: 2022, [Online], Available: https://keras.io.
24. Castaldi, G., V. Galdi, and G. Gerini, "Evaluation of a neural-networkbased adaptive beamforming scheme with magnitude-only constraints," *Progress In Electromagnetics Research B*, Vol. 11, 1–14, 2009.
25. Smida, A., R. Ghayoula, N. Nemri, et al., "Phased arrays in communication system based on Taguchineural networks," *Int. J. Commun. Syst.*, Vol. 27, No. 12, 4449–4466, 2014, https://doi.org/10.1002/dac.2625.
26. Jang, J.-S. R., "Self-learning fuzzy controllers based on temporal back propagation," *IEEE Trans. Neural Netw.*, Vol. 3, No. 5, 714–723, 1992, DOI: 10.1109/72.159060.
27. Vakula, D. and N. V. S. N. Sarma, "Using neural networks for fault detection in planar antenna arrays," *Progress In Electromagnetics Research Letters*, Vol. 14, 21–30, 2010, doi:10.2528/PIERL10030401.